nature astronomy

Article

https://doi.org/10.1038/s41550-023-01947-5

A history of mild shocks experienced by the regolith particles on hydrated asteroid Ryugu

In the format provided by the authors and unedited

Table of Contents

Supplementary Table 1. Molar fractions of Mg, Si+Al, and Fe of coarse-grained (typically >30 nm in width of packet) and fine-grained phyllosilicates (<30 nm in width) in the Ryugu particles by STEM-EDS analyses for Fig. 3d. Abbreviations: Ave. = average, S. D.= standard deviation.

A0002

Coarse-grained phyllosilicates

	Mg	Si+Al	Fe
	0.395	0.552	0.053
	0.399	0.545	0.056
	0.430	0.504	0.066
	0.397	0.526	0.077
	0.423	0.518	0.059
	0.394	0.539	0.067
	0.405	0.532	0.063
	0.425	0.512	0.063
	0.397	0.550	0.053
	0.419	0.523	0.057
	0.385	0.554	0.061
	0.393	0.545	0.062
	0.342	0.534	0.124
	0.385	0.545	0.070
	0.375	0.570	0.055
Ave.	0.398	0.537	0.066
S.D.	0.022	0.017	0.017

Fine-grained phyllosilicates

	Mg	Si+Al	Fe
	0.344	0.481	0.175
	0.338	0.481	0.181
	0.347	0.490	0.162
	0.349	0.486	0.165
	0.457	0.483	0.060
	0.407	0.472	0.121
	0.449	0.488	0.064
	0.439	0.494	0.068
	0.435	0.494	0.071
	0.432	0.492	0.076
	0.433	0.481	0.087
	0.447	0.487	0.066
	0.457	0.470	0.072
	0.432	0.494	0.074
	0.368	0.498	0.134
	0.336	0.476	0.187
	0.351	0.465	0.184
	0.349	0.469	0.181
	0.343	0.459	0.198
	0.341	0.468	0.191
	0.334	0.530	0.135
	0.315	0.560	0.124
	0.344	0.519	0.137
	0.314	0.554	0.131
	0.328	0.547	0.125
	0.306	0.546	0.148
	0.329	0.546	0.124
	0.348	0.569	0.083
	0.392	0.548	0.061
Ave.	0.375	0.502	0.124
S.D.	0.050	0.032	0.046

A0037

Coarse-grained phyllosilicates

	Mg	Si+Al	Fe
	0.404	0.537	0.060
	0.443	0.486	0.071
	0.424	0.507	0.069
	0.424	0.507	0.069
	0.395	0.544	0.061
	0.368	0.563	0.068
	0.359	0.571	0.070
	0.420	0.511	0.069
	0.413	0.523	0.064
Ave.	0.406	0.528	0.067
S.D.	0.026	0.027	0.004

Fine-grained phyllosilicates

	Mg	Si+Al	Fe
	0.437	0.499	0.064
	0.443	0.488	0.069
	0.418	0.509	0.073
	0.350	0.547	0.103
	0.359	0.528	0.114
	0.432	0.482	0.086
	0.388	0.527	0.085
	0.475	0.450	0.075
	0.426	0.513	0.061
	0.397	0.499	0.105
Ave.	0.413	0.504	0.084
S.D.	0.037	0.026	0.017

C0009

Coarse-grained phyllosilicates

	Mg	Si+Al	Fe
	0.318	0.486	0.196
	0.365	0.439	0.196
	0.352	0.454	0.194
	0.345	0.451	0.204
	0.339	0.447	0.213
	0.358	0.421	0.221
	0.338	0.447	0.215
	0.319	0.454	0.226
	0.335	0.453	0.212
	0.307	0.495	0.198
Ave.	0.338	0.455	0.208
S.D.	0.018	0.020	0.011

Fine-grained phyllosilicates

	Mg	Si+Al	Fe
	0.319	0.512	0.169
	0.288	0.551	0.161
	0.260	0.572	0.169
	0.327	0.471	0.202
	0.281	0.523	0.196
	0.274	0.487	0.239
	0.302	0.545	0.153
	0.269	0.551	0.180
	0.295	0.521	0.184
	0.275	0.517	0.209
Ave.	0.289	0.525	0.186
S.D.	0.021	0.029	0.025

C0068

Coarse-grained phyllosilicates

	Mg	Si+Al	Fe
	0.387	0.531	0.082
	0.358	0.575	0.067
	0.393	0.542	0.065
	0.374	0.552	0.074
	0.386	0.552	0.063
	0.390	0.546	0.064
	0.381	0.553	0.066
	0.381	0.549	0.070
	0.386	0.551	0.063
	0.425	0.510	0.065
	0.386	0.537	0.077
Ave.	0.386	0.545	0.069
S.D.	0.015	0.015	0.006

Fine-grained phyllosilicates

	Mg	Si+Al	Fe
	0.343	0.581	0.076
	0.348	0.591	0.061
	0.336	0.601	0.063
	0.324	0.601	0.075
	0.330	0.595	0.075
	0.336	0.585	0.079
	0.341	0.568	0.091
	0.342	0.596	0.062
	0.335	0.598	0.067
	0.390	0.538	0.072
	0.344	0.591	0.065
	0.335	0.580	0.085
	0.356	0.571	0.073
	0.361	0.571	0.068
	0.367	0.563	0.071
	0.383	0.551	0.066
Ave.	0.348	0.580	0.072
S.D.	0.018	0.018	0.008

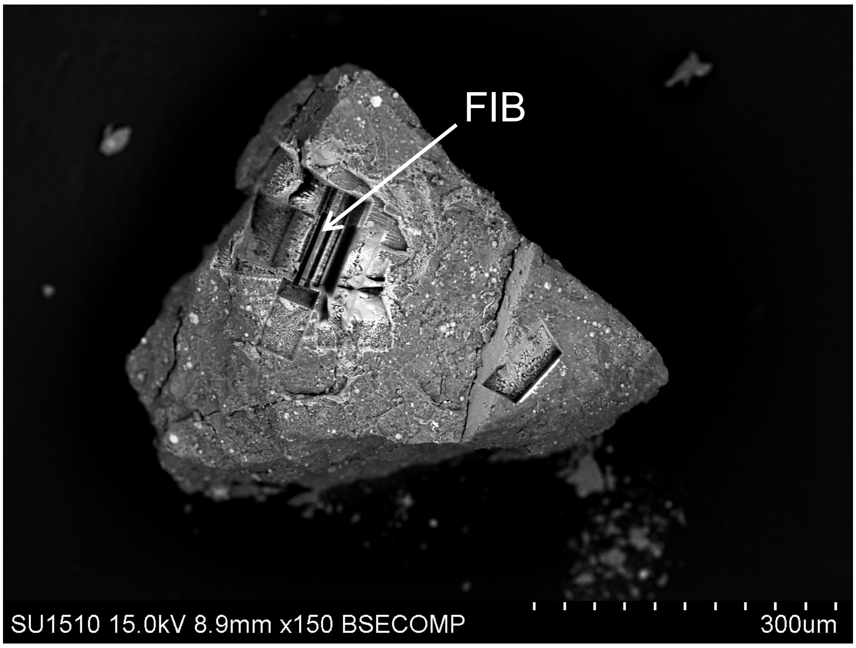

Supplementary Figure 1. Back-scattered electron image of a fragment from the A0002 particle placed on carbon tape. The portion for the ultrathin section of Supplementary Fig. 2a is indicated by an arrow.

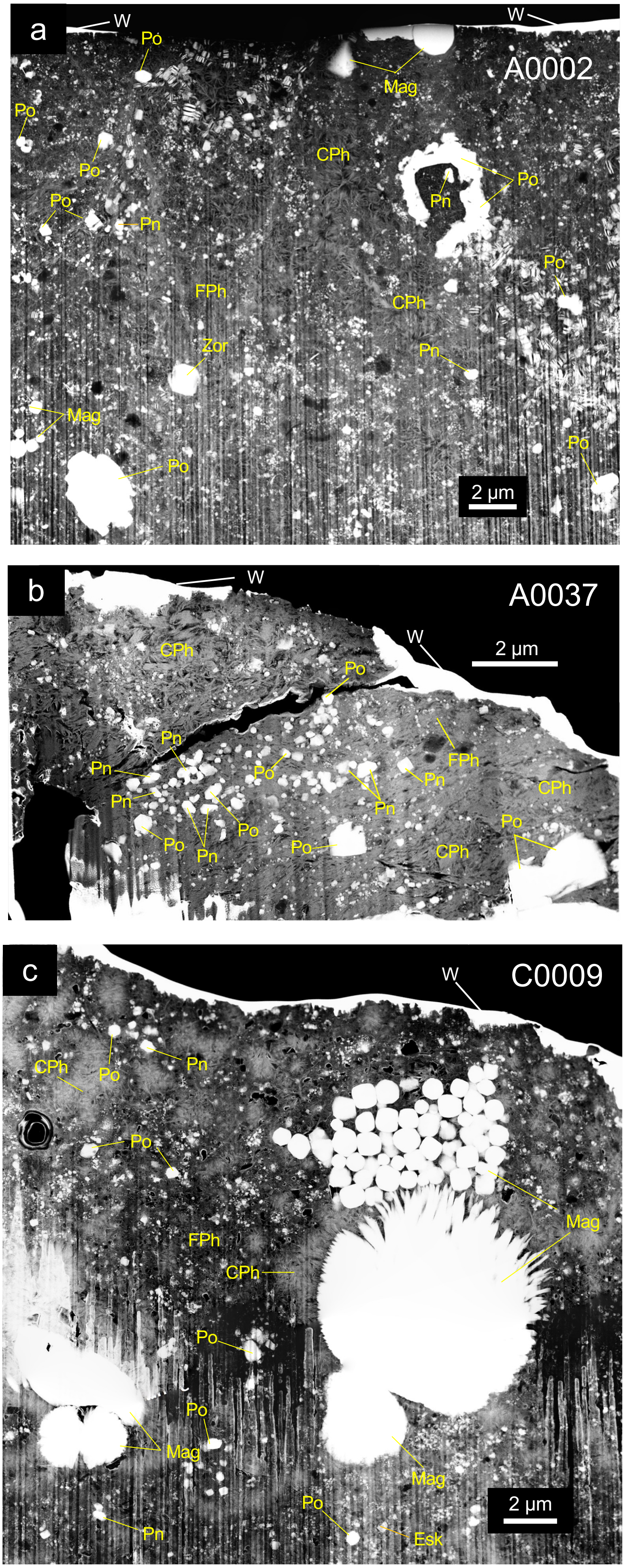
a
A0002
W
W
Po
Mag
Po
CPh
Po
Pn
Po
Po
Pn
Po
FPh
CPh
Zor
Pn
Mag
Po
Po
2 µm
b
A0037
W
W
2 µm
CPh
Po
Pn
Pn
Po
FPh
Pn
CPh
Pn
Pn
Po
Po
Pn
Po
CPh
Po
c
C0009
W
CPh
Po
Pn
Po
Mag
FPh
CPh
Po
Po
Mag
Mag
Po
Pn
Esk
2 µm

Supplementary Figure 2. High-angle annular dark-field scanning transmission electron microscope (HAADF-STEM) images of the ultrathin sections of Ryugu particles. Ultrathin sections were extracted from particles (a) A0002, (b) A0037, and (c) C0009 by a focused ion beam (FIB) instrument. All the sections consist mainly of phyllosilicates embedding Fe-sulfides and Fe-oxide. Abbreviations: CPh = coarse-grained phyllosilicate aggregate, FPh = fine-grained phyllosilicates matrix, Po = pyrrhotite, Pn = pentlandite, Mag = magnetite, Zor = zolenskyite, Esk = eskolaite, W = tungsten (protection layer).

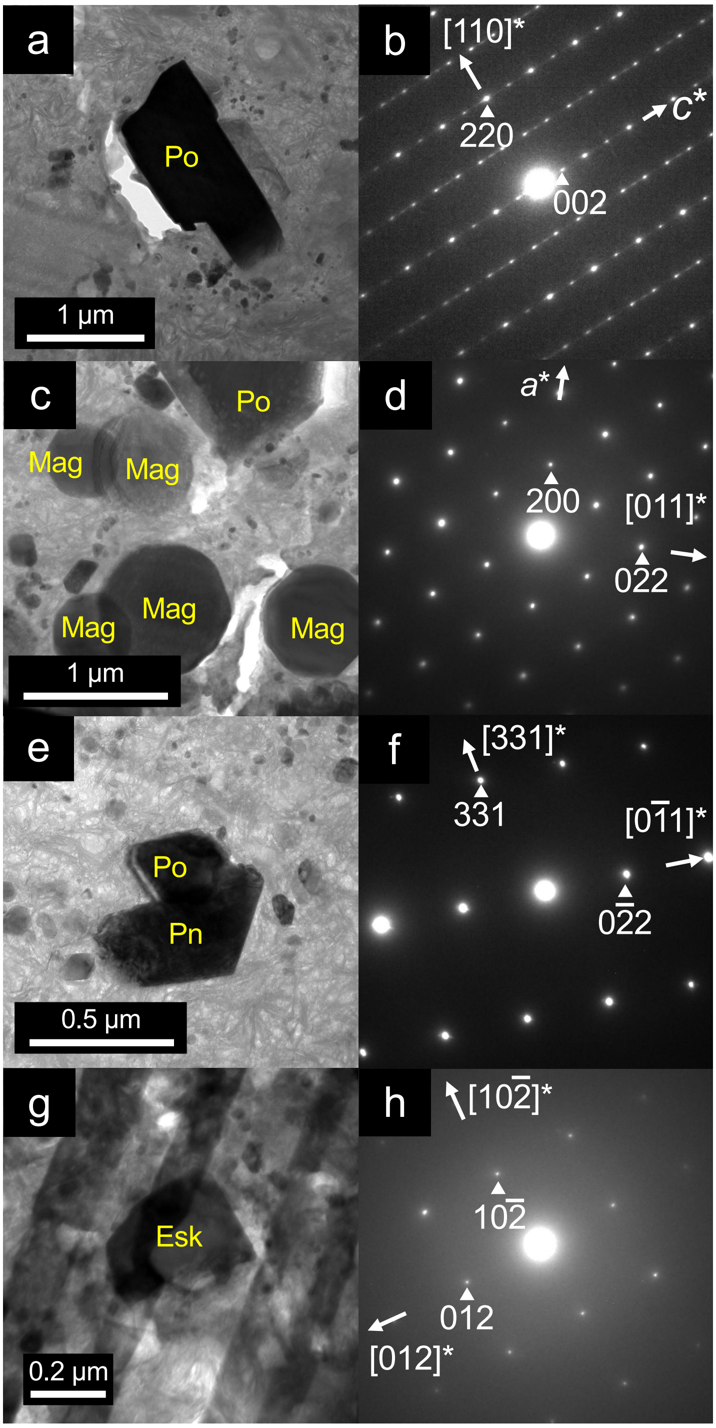

Supplementary Figure 3. Sulfides and oxides in the phyllosilicate matrices of Ryugu particles. BF-TEM images (a, c, e, g) and SAED patterns (b, d, f, h) of pyrrhotite (Po), magnetite (Mag), pentlandite (Pn), and eskolaite (Esk), respectively. SAED pattern of pyrrhotite shows the 4*C* polytype structure.

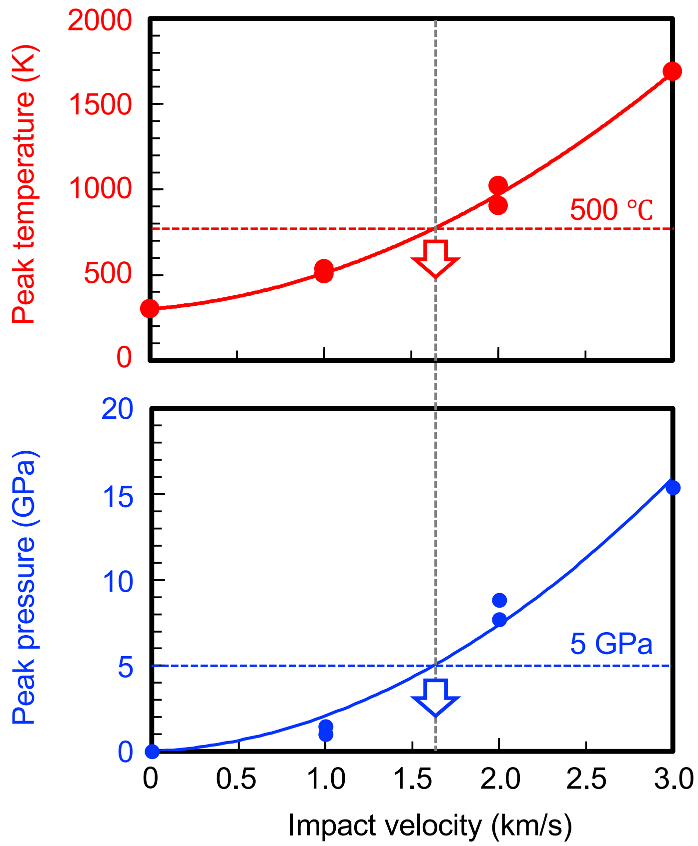

Supplementary Figure 4. Estimation of peak pressure and peak temperature of Ryugu particles by impact. Impact velocity – peak pressure – peak temperature relationships of a model hydrated carbonaceous chondrite based on numerical calculations ["Mean matrix pressures" and "Mean matrix temperatures" from Table 1 in Bland et al. (2014)[46]]. The model material has an initial volume fraction of serpentine matrix and olivine chondrules of 70:30 and an initial matrix porosity (ϕ) of 0.60–0.70. If the shock impedance of Ryugu materials is assumed to be comparable to that of CM chondrites, the upper bound of peak pressure for the Ryugu materials is at most ~5 GPa at the maximum peak temperature of ~500 °C considering non-dehydrated Mg-Fe serpentine.

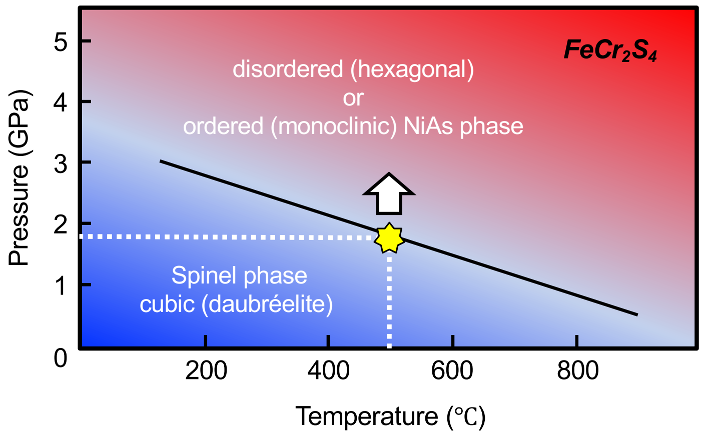

Supplementary Figure 5. Phase diagram of $FeCr_2S_4$. The diagram is modified after Tressler et al. (1968)[47]. Spinel-phase (daubréelite) is stable under ambient conditions. The disordered NiAs-phase (hexagonal) or ordered NiAs-phase (monoclinic: zolenskyite) are stable at higher pressures. Given that the average shock heating temperature of Ryugu particles is below ~500 °C corresponding to the breakdown temperature of Mg-Fe serpentine[45], daubréelite transforms into zolenskyite above ~2 GPa.

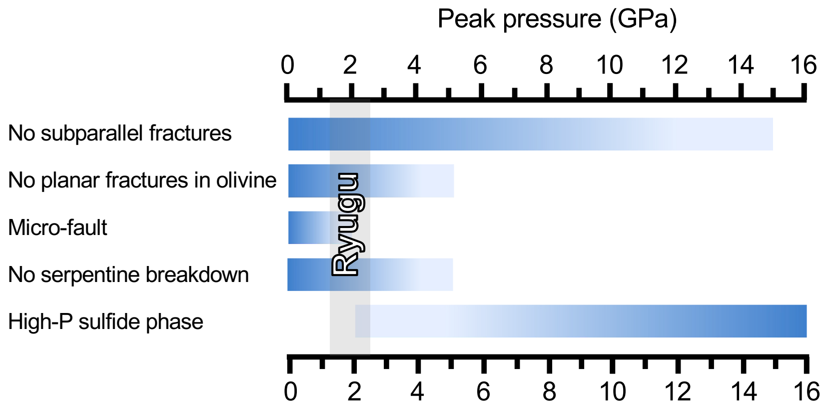

Supplementary Figure 6. Peak pressure estimation of Ryugu particles. The diagram shows the peak pressure ranges of shock metamorphism based on brittle deformations of bulk rocks and olivine grains, and phase transformations of Mg-Fe serpentine and Fe-Cr-sulfide.

Evaluation of peak pressure during the small carry-on impactor (SCI) cratering

Supplementary Text 1. Sampling probability of highly-shocked ejecta due to the SCI impact

We identified the shock features corresponding to peak pressure of ~2 GPa, in the Ryugu particles derived from the chamber C. The samples in the chamber C were collected from the touch down 2 (TD2) site where is ~20 m away from the artificial crater due to the small carry-on impactor (SCI)[63]. In this section, we estimated the volume fraction of the materials compressed up to 2 GPa to the total excavated volume during the SCI impact using shock physics modeling. The volume fraction would be approximated to be the probability that the shocked particles analyzed in this study is the SCI ejecta.

Here, we estimated the total volume of the SCI ejecta. Honda et al. (2021)[64] investigated the distribution of the deposited SCI ejecta blanket around the crater. A number of boulders larger than a few tens cm were newly discovered after the SCI impact. A fine-grained portion of the SCI ejecta, which were observed as an ejecta curtain[63] and mainly composed of the particles larger than 1 mm, formed a continuous ejecta blanket[65]. The thickness h of the blanket was presented as a function of the distance from the crater rim r as

$$h(r) = h_r \exp\left[-\frac{\left(\frac{r}{R_{rim}} - 1\right)}{\lambda_{rim}}\right], \text{ (S1)}$$

where h_r = 0.475 m and λ_{rim} = 0.245 are fitting constants, and R_{rim} = 8.8 m is the half of the rim-to-rim diameter of the SCI crater. By assuming axial symmetry, the total excavated volume from the SCI crater V_{exc} can be calculated as

$$V_{exc} = 2\pi \int_{R_{rim}}^{\infty} h(r) r \mathrm{d}r. \text{ (S2)}$$

Supplementary Fig. 7 shows h and the cumulative excavated volume as a function of r. Since h decays exponentially, the cumulative excavated volume asymptotically becomes a constant value, that is, V_{exc}. Consequently, we obtained V_{exc} to be 71 m^3, which is the excavated volume excluding the contribution from the boulders ejected during the SCI impact.

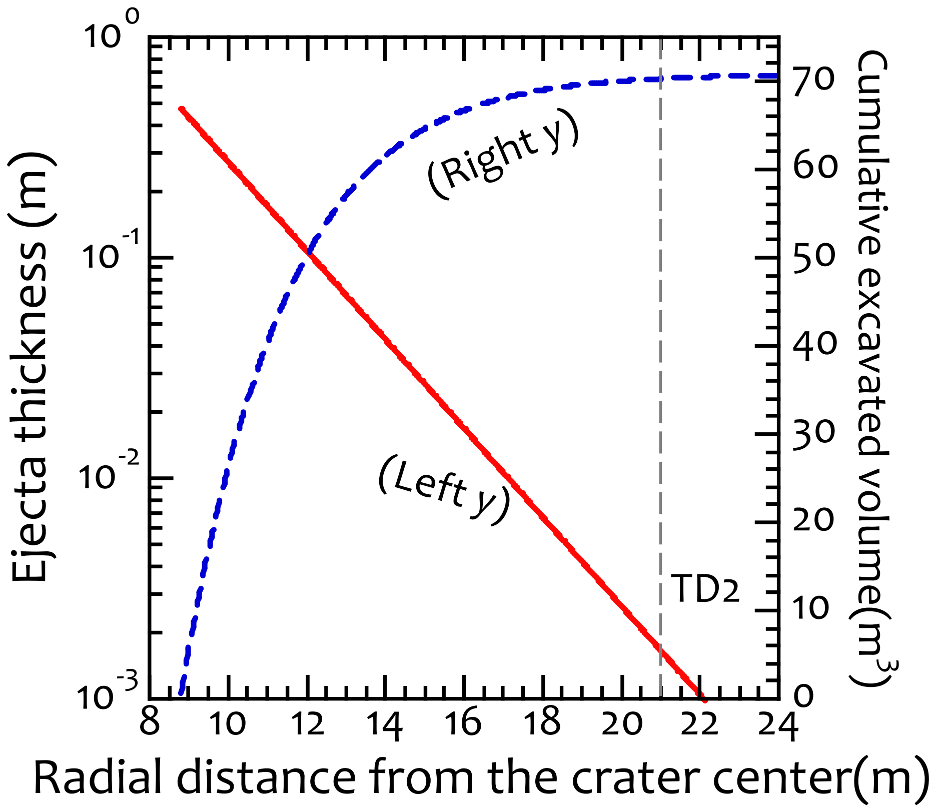

Supplementary Figure 7. SCI ejecta volume estimate. Ejecta thickness (left *y*, red solid) and cumulative excavated volume (right *y*, blue dashed) as a function of the radial distance from the center of the SCI crater. The radial distance of the TD2 site is also shown as the grey dashed vertical line.

We estimated the total volume of the shocked materials up to 2 GPa due to the SCI impact. We used the two-dimensional version of the iSALE shock physics code[66-68], iSALE-Dellen[69]. A cylindrical coordinate was employed. We modeled the SCI impact based on the dimensions of the impactor[63]. The SCI is a hollow sphere with the diameter of 130 mm and the thickness of 5 mm. The mass and the effective density are 2 kg and 1.7 Mg m^{-3}. Although the impact angle was ~60 degrees measured from the horizontal, we assumed vertical impacts in this study. This simplification leads to somewhat higher peak pressures in the target materials. Since the SCI was made of copper, we used the Tillotson equations of state (EOS) for copper[70] and the Johnson-Cook strength model with the parameters of copper[71]. Although concrete EOS models for carbonaceous asteroids have not been established, we used six material models pertaining to the Ryugu materials to examine the possible uncertainties. Nakamura et al. (2022)[31] constructed the EOS models with two different compressibility, which are referred to as "Ryugu hard" and "Ryugu soft", based on the physical properties of the Ryugu particle C0002. Unfortunately, the shock Hugoniot parameters of the Ryugu particle were not measured due to the limitation of the sample volume. Thus, Nakamura et al. (2022)[31] also constructed the two EOS models for the Murchison carbonaceous chondrite, which are called "Murchison bulk" and "Murchison solid", based on the Shock Hugoniot data of Murchison[72], for reference purposes. The EOS for "Murchison solid" is used by combining with porosity compaction models. We used the ε–α model[68] to treat the effect of porosity compaction on impact outcomes. We employed three initial densities, which are 1.2 Mg m^{-3}, 1.82 Mg m^{-3}, 2.2 Mg m^{-3}, by changing the initial porosity. The three densities correspond to the bulk density of Ryugu[73], the bulk density of the Ryugu grain C0002[31], and the bulk density of Murchison. Since we employed the six models with a range of initial density and compressibility, the true value would fall within the range of the impact outcomes. The material model parameters are summarized in Supplementary Tables 2 and 3. Note that we neglected the strength in the Ryugu materials. Shear deformation in the impact-driven flow converts from the kinetic energy to the internal energy due to plastic work, leading to an efficient decay of the peak pressure with increasing distance. Thus, the hydrodynamic assumption provides an upper bound of the shocked volume up to 2 GPa.

Supplementary Table 2. The material model parameters for the SCI. The parameters are the same used in Kadono et al. (2022)[74]. A detailed description of each parameter can be found in the iSALE manual[69].

Name	Copper
EOS model	Tillotson EOS
Poisson's ratio	0.3
Melting temperature (K)	1,356
Simon parameter *a* (GPa)	49.228
Simon parameter *b*	1.027
Specific heat (kJ K^{-1} kg^{-1})	0.3925
Johnson-Cook parameter *A* (MPa)	90
Johnson-Cook parameter *B* (MPa)	292
Johnson-Cook parameter *N* (MPa)	0.31
Johnson-Cook parameter *C* (MPa)	0.025
Johnson-Cook parameter *m* (MPa)	1.09
Reference temperature (K)	293

Supplementary Table 3. Same as supplementary Table 2, except that the parameters for the Ryugu materials (i.e., target materials) are summarized. A detailed description of each parameter can be found in the iSALE manual[69].

Name	Ryugu hard	Ryugu soft	Murchison bulk	Murchison solid	Murchison solid	Murchison solid
EOS model	Tillotson EOS	Tillotson EOS	Tillotson EOS	Tillotson EOS	Tillotson EOS	Tillotson EOS
Poisson's ratio	0.5	0.5	0.5	0.5	0.5	0.5
Initial density (Mg m^{-3})	1.82	1.82	2.2	2.2	1.82	1.2
Initial distension[a]	Not used.	Not used.	Not used.	1.19	1.459	2.232
Elastic threshold[a]	Not used.	Not used.	Not used.	-10^{-5}	-10^{-5}	-10^{-5}
Transition strain[a]	Not used.	Not used.	Not used.	1	1	1
Rate of porous[a] compaction	Not used.	Not used.	Not used.	0.98	0.98	0.98
Sound speed ratio[a]	Not used.	Not used.	Not used.	0.62	0.62	0.62

[a]The input parameters of the ε–α porosity compaction model.

The number of cells per SCI thickness (n_{CST}) is one of important parameters to accurately estimate peak pressure distribution because it is thinnest portion of the projectile. In this study, we employed n_{CST}= 10 as a fiducial value, resulting in 130 cells per the SCI radius. It is not practical to perform calculations until the crater formation is completed under the micro gravity environment on Ryugu (~500 s)[63]. Since the propagation of a compressive pulse occurs at the very early stage during impact events, we continued the numerical integration up to 0.58 ms because the total shocked mass experiencing >2 GPa compression does not change after this time. We can neglect the gravity at this time scale. The calculation settings are summarized in Supplementary Table 4.

Supplementary Table 4. Calculation setting used in the iSALE simulations. A detailed description of each parameter can be found in the iSALE manual[69].

Computational geometry	Cylindrical coordinates
The number of cells per the SCI thickness n_{CST}	5, 10, 20
Number of computational cells in the *R* direction	300 (n_{CST} = 5)
	600 (n_{CST} = 10)
	1200 (n_{CST} = 20)
Number of computational cells in the *Z* direction	1,000 (n_{CST} = 5)
	2,000 (n_{CST} = 10)
	4,000 (n_{CST} = 20)
Number of cells for the extension in the *R* direction	200
Number of cells for the extension in the +*Z* direction	200
Number of cells for the extension in the -*Z* direction	200
Grid spacing (mm/cell)	1 (n_{CST} = 5)
	0.5 (n_{CST} = 10)
	0.25 (n_{CST} = 20)
Location of the target surface[a]	800 cells(n_{CST} = 5)
	1,600 cells (n_{CST} = 10)
	3,200 cells (n_{CST} = 20)
Artificial viscosity a_1	0.24
Artificial viscosity a_2	1.2
Impact velocity (km s^{-1})	2.06
Initial temperature (K)	300[b]
High-speed cutoff	Double the impact velocity
Low-density cutoff (kg m^{-3})	100

[a]Measured from the bottom of the computational domain.

[b]Simaki et al. (2020)[75]

Supplementary Fig. 8 shows the peak pressure distribution in the case with the Ryugu hard model on a provenance plot and on a snapshot at the time of 0.58 ms. We found that the strongly shocked region with the peak pressure higher than 2 GPa is limited mostly to the SCI footprint. The other models provide similar results. Supplementary Fig. 9 shows the cumulative volume experiencing the compression up to a given peak pressure as a function of peak pressure. We found that the model dependence of the shocked volume is not large at least around 2 GPa, and that the volume fraction of the SCI ejecta experiencing >2 GPa compression to the total excavated volume from the SCI crater is only (1.7–3.4) x 10^{-5}. This value might be an upper bound of the probability that the shocked sample analyzed in this study is one of the SCI ejecta because of the following reasons. The highly shocked materials during the SCI impact are likely to be displaced and buried into the crater floor rather than excavation as shown in the snapshot of the simulation (Supplementary Fig. 8). In addition, the assumptions of the vertical impact and of purely hydrodynamic tend to provide an overestimation in peak pressure distribution as mentioned above. Consequently, the possibility that the shock feature found in this study was produced during the SCI impact is unlikely although we cannot rule out the possibility in principle.

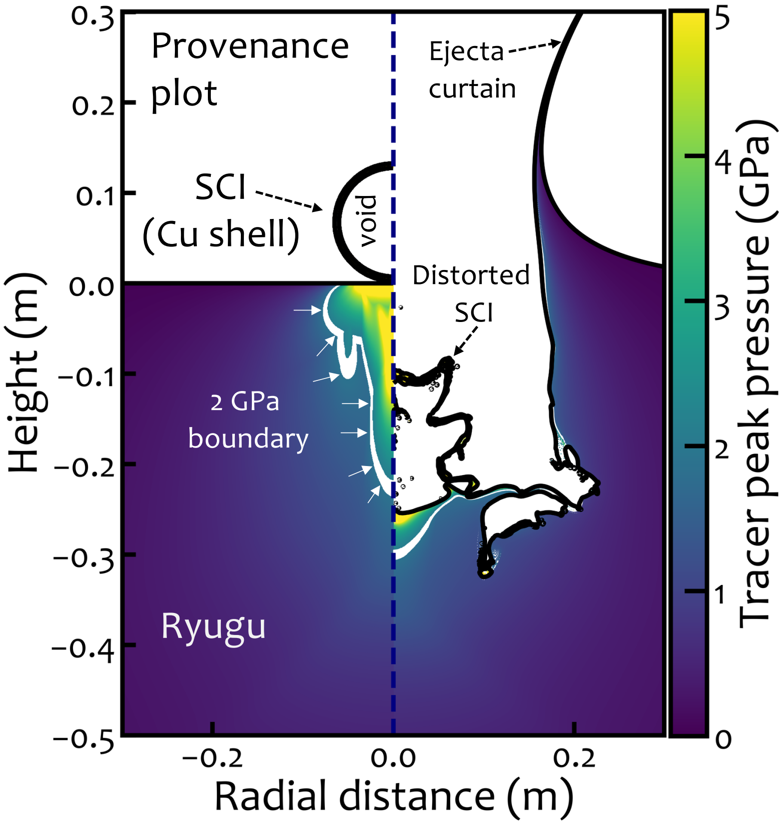

Supplementary Figure 8. Numerical results. The peak pressure distribution on a provenance plot (left) and on a snapshot. The color bar indicates the tracer peak pressure. The time of these plots is 0.58 ms after the impact. The boundary of 2 GPa compression is shown in the figure as the white line and indicated by white arrows.

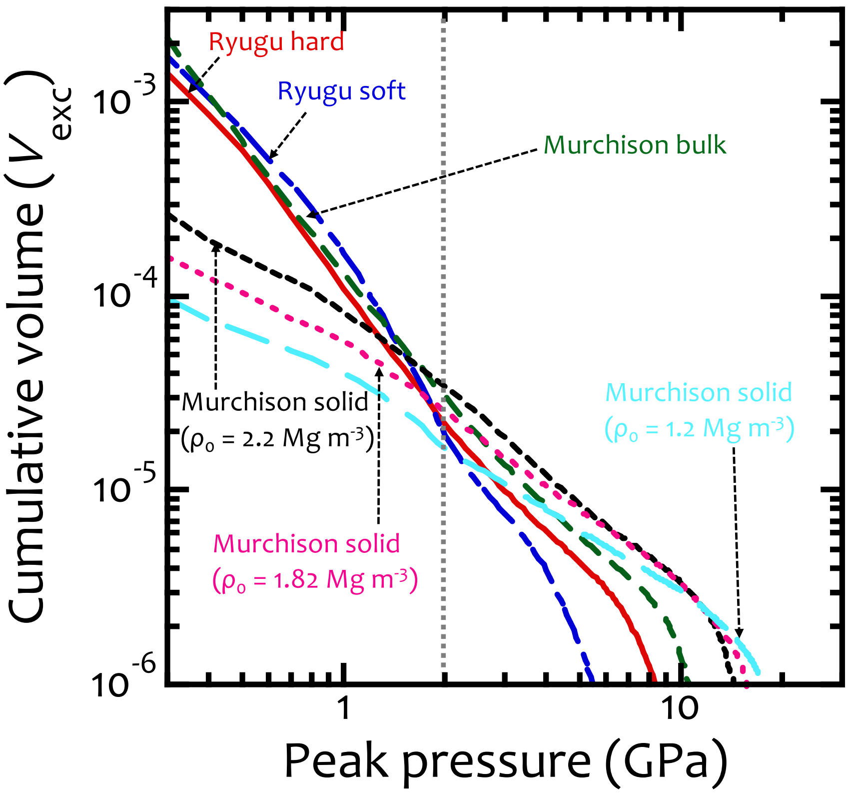

Supplementary Figure 9. Shocked volume. The cumulative volume of the materials compressed to a given peak pressure as a function of peak pressure. The volume is normalized by the total excavated volume during the SCI impact. The name of the material model used to obtain each line is indicate beside the line.

Supplementary Text 2. Resolution effect on impact outcomes

It has been widely known that spatial resolution employed in impact simulations affects the outcomes [e.g., 76]. Thus, we should address the resolution effects. We conducted additional two runs with the Ryugu hard model with half and two-fold n_{CST} value (5 and 20) to investigate the robustness of Supplementary Fig. 9 with respect to the change in spatial resolution. Supplementary Fig. 10 shows the same as Supplementary Fig. 9, except that the results of the resolution test are shown. We confirmed that three lines with different n_{CST} values mostly converge into a single line at least around 2 GPa. Consequently, the shocked volume estimate shown in Supplementary Text 1 is expected to be robust, and the selection of the fiducial value ($n_{CST} = 10$) is appropriate.

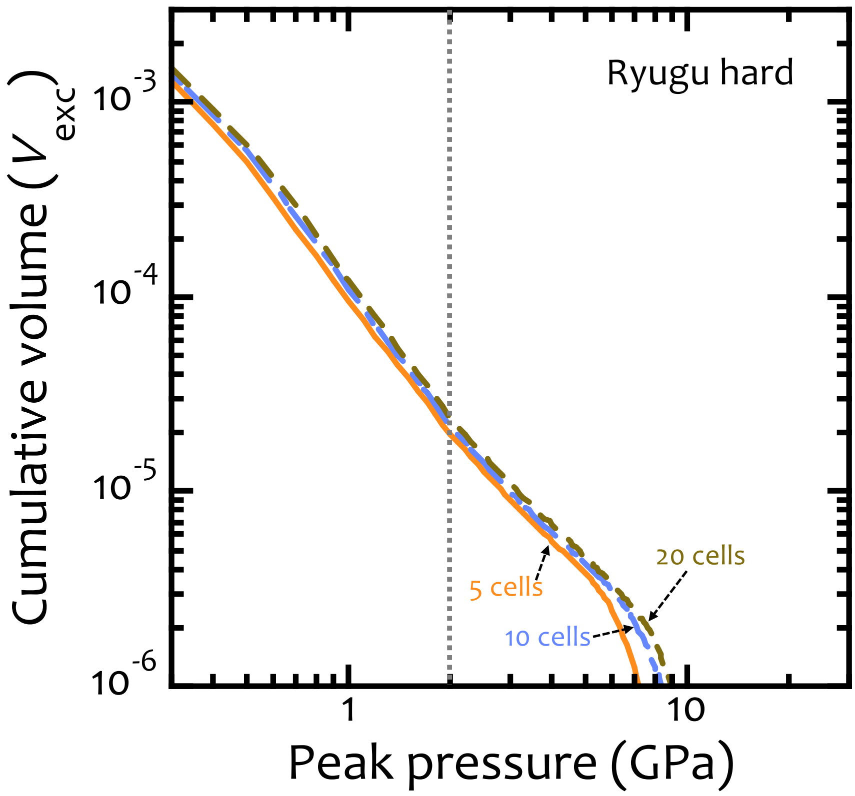

Supplementary Figure 10. Resolution effects. The same as Supplementary Fig. 9, except that the Ryugu hard model was only used and the three different values of the number of cells per the SCI thickness (n_{CST}) were used.

Supplementary Text 3. Maximum stress during sampling operation

The Hayabusa2 spacecraft conducted sampling operations two times during the mission. A tantalum projectile was accelerated up to 300 ± 30 m s^{-1} and impacted onto the Ryugu surface within a sampler horn[77]. The ejected particles were collected and analyzed in this study. In this section, we address the maximum stress during the sampling operation. The impact velocity is much slower than the bulk sound speed of the Ryugu samples[31]. The maximum longitudinal stress σ_L under the sub-sonic regime can be calculated as Melosh (1989)[78],

$$\sigma_L = \rho_0 V_P u_p, \quad (S3)$$

where ρ_0 is the bulk density, V_P is the longitudinal sound speed, and u_p is particle velocity behind the compressive wave. The physical properties ρ_0 and V_P were measured by Nakamura et al. (2022)[31] to be 1.82 Mg m^{-3} and 2.08 km s^{-1}, respectively. If we replace u_p with the impact velocity, the equation (S3) provides the upper bound of the longitudinal stress during the sampling operation, resulting in that the maximum stress produced in the collected samples is calculated to be 1.3 GPa, which is smaller than the pressure of the Ryugu particle inferred from the sample analyses performed in this study.

References only in Supplementary Information

63. Arakawa, M. et al. An artificial impact on the asteroid 162173 Ryugu formed a crater in the gravity-dominated regime. *Science* **368**, 67–71, doi.org/10.1126/science.aaz1701 (2020).

64. Honda, R. et al. Resurfacing processes on asteroid (162173) Ryugu caused by an artificial impact of Hayabusa2's small carry-on impactor. *Icarus* **366**, 114530, doi.org/10.1016/j.icarus.2021.114530 (2021).

65. Wada, K. et al. Size of particles ejected from an artificial impact crater on asteroid 162173 Ryugu, *Astron. Astrophys.* **647**, A43, doi.org/10.1051/0004-6361/202039777 (2021).

66. Amsden, A., Ruppel., H. & Hirt, C. SALE: A simplified ALE computer program for fluid flow at all speeds. *Los Alamos National Laboratories Report*, LA-8095:101p. (1980).
67. Ivanov, B. A., de Niem, D. & Neukum, G. Implementation of dynamic strength models into 2-D hydrocodes: Applications for atmospheric breakup and impact cratering. *Int. J. Impact Eng.* **20**, 411–430, doi.org/10.1016/S0734-743X(97)87511-2 (1997).
68. Wünnemann, K., Collins, G. S. & Melosh, H. J. A strain-based porosity model for use in hydrocode simulations of impacts and implications for transient crater growth in porous targets. *Icarus* **180**, 514–527, doi.org/10.1016/j.icarus.2005.10.013 (2006).
69. Collins, G. S. et al. iSALE-Dellen manual. Figshare, doi.org/10.6084/m9.figshare.3473690.v2 (2016).
70. Tillotson, J. H. Metallic equations of state for hypervelocity impact. Technical Report *GA-3216*, *General Atomic Report* (1962).
71. Johnson, G. R. & Cook, W. H. A constitutive model and date for metals subjected to large strains, high strain rates and high temperatures. Seventh International Symposium on Ballistics, Hague (1983).
72. Anderson, W. W. & Ahrens, T. J. Shock wave equations of state od chondritic meteorites. *AIP Conf. Proc.* **429**, 115–118, doi.org/10.1063/1.55475 (1998).
73. Watanabe, S. et al. Hayabusa2 arrives at the carbonaceous asteroid 162173 Ryugu-A spinning top-shaped rubble pile. *Science* **364**, 268–272, doi.org/10.1126/science.aav8032 (2019).
74. Kadono, T. et al. Effect of projectile shape and interior structure on crater size in strength regime. *Earth, Planets, Space* **74**:132, doi.org/10.1186/s40623-022-01690-7 (2022).
75. Shimaki, Y. et al. Thermophysical properties of the surface of asteroid 162173 Ryugu: Infrared observations and thermal inertia mapping. *Icarus* **348**, 113835, doi.org/10.1016/j.icarus.2020.113835 (2020).
76. Pierazzo, E. et al. Validation of numerical codes for impact and explosion cratering: Impacts on strengthless and metal targets. *Meteoritics & Planetary Science* **43**, 1917–1938, doi/10.1111/j.1945-5100.2008.tb00653.x (2008).

77. Tachibana, S. et al. Pebbles and sand on asteroid (162173) Ryugu: In situ observation and particles returned to Earth. *Science* **375**, 1011–1016, doi.org/10.1126/science.abj8624 (2022).
78. Melosh, H. J. Impact cratering: a geologic process. pp.29, Oxford University Press, New York (1989).